BN/GdxTi(1-x)O(4-x)/2 nanofibers for enhanced photocatalytic hydrogen production under visible light

Amr Nada, Maged Bekheet, Roman Viter, Philippe Miele, Stéphanie Roualdes, Mikhael Bechelany

HAL Id: hal-02146530

https://hal.umontpellier.fr/hal-02146530v1

Submitted on 31 May 2021

BN/Gd$_x$Ti$_{(1-x)}$O$_{(4-x)/2}$ nanofibers for enhanced photocatalytic hydrogen production under visible light

Amr A. Nada [a,b]**, Maged F. Bekheet** [c,d]**, Roman Viter** [e]**, Philippe Miele** [b]**, Stéphanie Roualdes** [b] **and**

Mikhael Bechelany [b]

[a] Dept. of Analysis and Evaluation, Egyptian Petroleum Research Institute, Cairo, Nasr city P.B. 11727, Egypt.

[b] Institut Européen des Membranes, IEM – UMR 5635, ENSCM, CNRS, Univ Montpellier, Montpellier, France

[c] Fachgebiet Keramische Werkstoffe / Chair of Advanced Ceramic Materials, Institut für Werkstoffwissenschaften und -technologien, Technische Universität Berlin, Hardenbergstraße 40, 10623 Berlin, Germany

[d] Department of Material Science Engineering, University of Utah, 122 Central Campus Dr., Salt Lake City, UT 84112, USA

[e] Institute of Atomic Physics and Spectroscopy, University of Latvia, 19 Raina Blvd., LV 1586 Riga, Latvia

ABSTRACT

BN/Gd$_x$Ti$_{(1-x)}$O$_{(4-x)/2}$ nanofibers were elaborated via electrospinning technique. The properties of the prepared nanofibers were controlled using different ratios of gadolinium. All the prepared nanofibers exhibit the tetragonal structure of anatase TiO$_2$ phase. An increase in the unit cell volume and a decrease in the crystallite size were observed with increasing the doping amount of Gd^{3+} as revealed by Rietveld refinement analysis. The defect in TiO$_2$ lattice was observed by Raman. The Gd^{3+} incorporation inside TiO$_2$ lattice, which is accompanied by the creation of Ti-O-Gd bond, was characterized by the X-ray photoelectron spectra. Scanning electron microscopy demonstrates that the average diameter of BN/Gd$_x$Ti$_{(1-x)}$O$_{(4-x)/2}$ nanofibers decreased by 0.1 µm in comparison to nanofibers without doping. The d-spacing raised by 0.01 nm after doping as

demonstrated by high-resolution transmission electron microscopy. The distribution of BN and Gd^{3+} was homogenous and uniform on nanofibers as depicted by EDX. The incorporation of many impurity levels between valence band and conduction band enhanced absorptivity under visible light as revealed by UV−visible spectrophotometry. Moreover, the surface area of nanofibers was improved by 5 times after Gd^{3+} doping as demonstrated by BET which is favorable for the increase of photocatalytic activity. The electrons transfer rate (recorded by the electrochemical impedance spectroscopy analysis) was improved by gadolinium doping as well. The photocatalytic results indicate that the $BN/Gd_xTi_{(1-x)}O_{(4-x)/2}$ nanofibers improve hydrogen production up to 192602 ± 1500 µmole/g during 6 hours under visible light. The $BN/Gd_xTi_{(1-x)}O_{(4-x)/2}$ nanofibers produced 7 times more hydrogen than nanofibers without BN. This improvement could be attributed to the e^-/h^+ stability that reached 63.69 ms average time before recombination due to the beneficial effect of BN nanosheets.

INTRODUCTION

Since many decades, the energy issues have a major global matter. One challenge to prevent the climate change is to find another suitable alternative fuel than the depleted fossil fuel. The photocatalytic technology using semiconductors provides an easy way to produce hydrogen as a competitive alternative fuel [1,2]. Various semiconductors have been used as photocatalysts for water treatment [3–6] and hydrogen production such as $BiVO_4$, NiO, WO_3, Cu_2O, CdS and TiO_2 [7–11].

Among them, titanium dioxide (TiO_2) is effective as photocatalyst for water splitting because it is stable, environmentally friendly and inexpensive [12–14]. Nevertheless, TiO_2 presents the disadvantage to get a relatively large optical band gap limiting its activity in the visible range

[15]. Moreover, TiO_2 is characterized by a charge recombination time (10^{-9} s) which is higher than the time required for chemical interaction of adsorbed molecules on it (10^{-3} to 10^{-8} s) [16,17]. To overcome these limitations, different attempts have been made to create oxygen vacancies in TiO_2 lattice which can proficiently shift the response of TiO_2 into the visible region [18,19]. As a striking example, the photocurrent of TiO_2 was enhanced by doping TiO_2 with lanthanide (especially gadolinium (Gd)) in previous studies [20,21] where electrons stabilization mechanism of 4f state in Gd improves the electron transfer in titania [22]. The limitation of e^-/h^+ recombination in TiO_2 has been overcome by doping with carbon, other semiconductor or noble metals such as Graphene oxide [23], $ZnFe_2O_4$ [13], Fe_3O_4/Gd [24], Ag [25], La [26] and BN [27,28].

Combining hexagonal boron nitride (h-BN) with TiO_2 is one of the effective methods to enhance the separation between electrons and holes in TiO_2. BN has many unique stable properties such as high thermal stability and high chemical stability to be considered as a suitable support [29,30]. BN with high surface area could increase absorptivity of reactants [31] and it was used in a wide range of applications such as nanoelectronics and nanocomposites [32]. Despite that BN has similar structure to that of graphene structure, its B–N polar bonds enhance the photocatalytic efficiency more than that of C-C covalent bonds in graphene [27]. Previous studies demonstrate that the incorporation of BN sheets with TiO_2 nanofibers improves the separation of the photo-induced electrons and holes in titanium dioxide nanofibers with compared to that of the pristine nanofibers [27,28].

Several Gd-Ti oxides, which contain high amount of Gd such as $Gd_2Ti_2O_7$ [33], TiO_2/Gd_2O_3/Pt [34] $Gd_2Ti_{0.6}Mo_{1.2}Sc_{0.2}O_{7-\delta}$ [35] and $Gd_2Ti_2O_7$/$GdCrO_3$ [36], have been reported to show high photocatalytic activity for hydrogen production under UV and visible light. The high amount of

gadolinium has been used in previous oxides which has been conflicted with the scarcity and high cost of gadolinium. For example, only one work has been reported on the photocatalytic hydrogen production of 2 wt% Gd and N co-doped TiO_2 [1]. Although Gd and N co-doped TiO_2 exhibit comparable photocatalytic activity to $Gd_2Ti_2O_7$, $TiO_2/Gd_2O_3/Pt$ and $Gd_2Ti_2O_7/GdCrO_3$ systems, they use methanol as sacrificial agent, which increases the costs of the process as well. The methanol is usually used to capture the hole on the TiO_2 that will indeed delay the electron−hole recombination of the photocatalyst. Introducing BN into the Gd doped TiO_2 photocatalyst is recognized as a cost-effective and emerging strategy, which could not only help the full utilization of the solar light energy but also act as hole capture agent instead of methanol, which profoundly facilitates the separation of the photo-induced electrons and holes in the TiO_2 nanofibers [27,28]. The bulk TiO_2 catalysts usually possess low specific surface areas due to the aggregation of their particles, thus, they suffer from the large band gap barrier and fast electron−hole recombination that lower their photocatalytic efficiency. In contrast, one-dimensional nanofibers usually show low aggregation tendency, and thus, large specific surface area, which allows sufficient reactive sites on the surface as well as facilitates the charge and mass transfer for enhanced photocatalytic activities, in particular for the heterostructured photocatalysts [37–39]. Accordingly, the main goal of this work is to apply electrospinning technique to prepare $BN/Ti_{1-x}Gd_xO_2$ (x ≤ 0.03) nanofibers with high amount of oxygen vacancy. The morphology, structure, and optical properties of the prepared fibers have been analyzed. The performance of these materials for hydrogen production under visible light has been also evaluated.

EXPERIMENTAL SECTION

1. **Materials**

Gadolinium nitrate ($Gd(NO_3)_3.6H_2O$, 99.99%), titanium tetraisopropoxide (TTIP) ($Ti(OCH(CH_3)_2)_4$) (97%), polyvinylpyrrolidone (PVP; Mw = 1300 000 g/mol), acetic acid (98%), absolute ethanol (99%), absolute methanol (99%) and gelatine from porcine skin were purchased from Sigma Aldrich. BN nanosheets were prepared from commercial BN (Saint Gobain, 95%, 325 mesh). All chemicals were used without any further purification.

2. **Exfoliation of BN**

Boron nitride nanosheets were elaborated from commercial boron nitride powder with gelatine [28]. 20 g of porcine skin gelatine was dissolved in 80 mL of hot water (75 °C). After dissolution of gelatine, 1 g of BN was added to the solution. The mixture was kept overnight in an ultrasonic homogenizer at 50 °C. Exfoliated BN was collected from last precipitates by centrifugation at 6000 rpm for 30 minutes and the supernatant was collected to repeat the separation process for two times more. The precipitates were dried at 80 °C for 48 hours and then calcined at 600 °C for 2 hours in air with a heating rate of 5 °C/min to obtain the pure exfoliated BN.

3. **Preparation of $BN@TiO_2$, $BN@Ti_{1-x}Gd_xO_{2-0.05x}$ and $Ti_{1-x}Gd_xO_{2-0.05x}$ composite nanofibers**

BN incorporated TiO_2 and BN incorporated $Ti_{1-x}Gd_xO_{2-0.05x}$ composite nanofibers were prepared using the electrospinning technique. The solution was prepared in three steps. Firstly, TTIP was dissolved in a mixture that contained 3 mL of ethanol, 2 mL of acetic acid and 0.3 g of PVP and stirred for 1h at room temperature (precursor solution). Secondly, different amounts of $Gd(NO_3)_3$ (0, 0.5, 1, and 1.5 and mole % refer to Gd^{3+}/Ti^{4+}) were dissolved in 2 mL of ethanol with 30 min

stirring to get BG0, BG0.5, BG1 and BG1.5 samples, respectively. The gadolinium solution was added dropwise to the precursor solution under continuous stirring for 30 min. Third solution, 15 mol% of exfoliated BN related to TiO_2 was sonicated in 2 mL ethanol for 12h then added to the precursor solution. For comparison 1 additional sample was prepared with 1.5 mole % of $Gd(NO_3)_3$ without the addition of BN nanosheets and was denoted G1.5. The homogeneous solution was transferred to a syringe with a nozzle of stainless-steel (diameter of 0.7 mm). The solution was controlled by a dosing pump with a constant flow rate of 1 mL/h. The temperature inside the chamber of electrospinning was 38 ±5°C. A high voltage power (1.25 kV/cm) was applied between the nozzle and the collector. Nanofibers were picked on a rotating coil covered with an aluminium foil with a rotation speed of 400 rpm. The composite nanofibers were collected and then calcined in a muffle furnace at 500 °C (heating rate: 5 °C/min) for 5 h in air.

4. Characterisations of nanofibers

The crystalline phase of the obtained nanofibers was analysed by X-ray diffraction (XRD), using a PANAlytical Xpert-PRO diffractometer equipped with an Xcelerator detector using Ni-filtered Cu-radiation with wavelength of 1.54 A. The scan step size of all prepared fibers was fixed at 0.0167 °/step and the time per step was 0.55 sec/step. Rietveld refinement was performed using the FULLPROF program [40] and profile function 7 (Thompson-Cox-Hastings pseudo-Voigt convoluted with axial divergence asymmetry function) [41]. The resolution function of the instrument was obtained from the structure refinement of silicon standard. More information about using pseudo-Voigt function to calculate the crystallite size and micro-strain is reported elsewhere [42]. The morphology of all nanofibers was studied via scanning electron microscopy (SEM) where images were taken with a Hitachi S4800, Japan. Energy-dispersive X-ray

spectroscopy analysis (EDX) and elemental mapping were performed with a Zeiss EVO HD15 microscope coupled with an Oxford X-MaxN EDX detector. The morphology and structure of the samples were also studied via high resolution transmission electron microscopy (HRTEM) on JEOL JEM 2100 (JEOL, Japan) at an accelerating voltage of 200 kV. Raman spectra were measured by the dispersive Raman spectroscopy (Model Sentera, Bruker, Germany) using 532 nm laser [doubled Nd:YAG laser (neodymium-doped yttrium aluminum garnet)] and a power of 10 mW. Fourier transform infrared (FTIR) spectra were detected via an ATR system on a Nicolet 370 FTIR spectrometer. The elemental composition of the prepared samples was investigated by X-ray photoelectron spectroscopy (XPS) on an Escalab 250 (Thermo Fisher Scientific, USA) using a monochromatic Al K Alpha (1486.6 eV) at 2kV and 1 µA. 400 µm of the surface diameter was analysed during an acquisition time of 1203.5 s. The band gab of nanofibers was measuring from UV-Vis spectra. These spectra were measured by a UV-Vis spectrophotometer (Jasco model V-570) equipped with a diffuse reflectance (DR) attachment (Shimadzu IRS-2200). The surface area of the nanofibers was detected from nitrogen adsorption–desorption isotherms at liquid nitrogen temperature using Micromeritics ASAP 2010 equipment (degassing conditions: $200^{\circ}C/12h$). The charge transport resistance and electron lifetime were measured by electrochemical impedance spectroscopy (EIS) for all prepared nanofibers. For that purpose, a thin layer of nanofiber was deposited on glass coated with indium tin oxide (ITO - 1 cm^2). A 0.5 M Na_2SO_4 was used as electrolyte with a three-electrodes cell (the obtained sample on ITO, Ag/AgCl and platinum wire as the working, reference and counter electrodes, respectively). The spectra of EIS were carried out at open circuit potential conditions under visible light of linear halogen lamp (500 mW; in the range of 420-600 nm) over a frequency range of 10^{-2} to 10^5 Hz. The EIS data were analysed and fitted to the proposed equivalent circuit by EC-Lab software.

5. Hydrogen Production evaluation

The photocatalytic H_2 evolution test was carried out in 50 mL of an air tight quartz reactor using 20 mL of 20% aqueous methanol solution (methanol as scavenger) with 50 mg of nanofibers. The reactor was sealed with a tight rubber septum (Aldrich) then it was purged with nitrogen gas to remove the dissolved gases in the solution. The solution was magnetically stirred in the dark for 30 min to establish the adsorption/desorption equilibrium. The aqueous solution and nanofibers were then irradiated by 500W linear halogen lamp (the visible light source is in the range of 420-600 nm) [13,43]. The temperature was kept at 25 °C by circulating water in a cylindrical tube surrounding the reactor during the experiment. The distance between the lamp and the aqueous solution was maintained at 10 cm. Every one hour, gas sample was collected by syringe to evaluate hydrogen and was monitored by gas chromatography (GC-1690, Jiedao, TCD, Ar carrier) with a 5 Å molecular sieve column (3 m × 2 mm).

6. Quantum efficiency calculation

Quantum Efficiency (QE) was calculated in order to present the catalytic results. QE was defined by equation 1 [44].

$$QE = \frac{2 \cdot N(H_2)}{N_{absorbed\ photons}} \qquad \text{equation (1)}$$

where *N(H2) and Nabsorbed photons* are number of hydrogen molecules and absorbed photons, respectively.

The number of hydrogen molecules can be calculated as:

$$N(H_2) = \mu(mol) \cdot 6.02 \cdot 10^{23} \qquad \text{equation (2)}$$

The number of absorbed photons was estimated in the following way:

$$N_{absorbed\ photons} = \sum_{400nm}^{800nm} \eta(\lambda) \cdot S \cdot \left(1 - e^{-\alpha(\lambda)}\right)/h\nu/e \quad \text{equation (3)}$$

Where λ, $\eta(\lambda)$, S, $\alpha(\lambda)$, $h\nu$, e are wavelength of incident light, power density of light with wavelength λ (W/m^2), area of the reactor, absorption coefficient, photon energy in eV and electron charge, respectively.

In fact, rough evaluations of the scattered light will allow to assume that the scattered light intensity will depend on nanofiber concentration, molar mass and refractive index as reported elsewhere [45]:

$$I \sim \frac{n_0^2 \cdot C \cdot M \cdot \dfrac{dn}{dC}}{\lambda^4} \quad \text{equation (4)}$$

Where I, n_0, C, M, dn/dC and λ are the scattered intensity, the refractive index of the solvent, the concentration of the nanofibers, the average molecular weight of the nanofibers, the change of the refractive index after adding of the nanofibers and the light wavelength, respectively. Refractive indexes of water, methanol, BN and TiO$_2$ in visible range are 1.33, 1.33, 2.17 and 2.6, respectively. Therefore, adding of the TiO$_2$ powder will increase the scattering. However, the scattering rate will be different for different wavelengths. Joshi *et al.* showed that in TiO$_2$ nanofibers, the backscattered light in visible range is minimal and the scattering angle 2θ is $\sim 60^{\circ}$ [46]. On the basis of the above mentioned, we can assume that the light scattering will reduce the quantum efficiency of the photocatalyst, however the experimental evaluation of this scattering will be a complex procedure and it is beyond the aim of this paper.

Result and discussion

The BN/TiO$_2$ (BG0) and the Gd doped BN/TiO$_2$ NFs with different amounts of gadolinium (BGX) were obtained by electrospinning of polymeric solution containing titanium tetraisopropoxide as precursor. X-ray diffraction (XRD) pattern of all prepared nanofibers are presented in Figure 1. The XRD reflections of all samples can be indexed to the tetragonal structure of anatase TiO$_2$ phase (JCPDS No. 01-084-1285) as present in Figure S1. The diffraction peak of h-BN (at 26 ^{o}) that corresponds to the (002) plan is overlapped with the diffraction peak of TiO$_2$ anatase at the same position [28]. No XRD reflections were observed for Gd$_2$O$_3$ and thus the substitution can be assumed to be close to random. These low doping amount of Gd^{3+} could uniformly substitute Ti^{4+} ions or occupy the interstitial sites in TiO$_2$ lattice [47]. However, the broadening and the slight shift of the XRD peak to lower 2θ angle with the increasing of Gd^{3+} ions doping amount may be ascribed to lattice distortion or lattice disparity in the crystal [48]. Therefore, the lattice parameters and the microstructure of the prepared samples were evaluated by Rietveld refinement. As presented in Table 1, an increase in the unit cell volume with increasing the amount of Gd^{3+} was observed, which can be explained by the substitution of smaller Ti^{4+} by larger Gd^{3+} ions (r (Ti^{4+}) = 60.5 pm, r (Gd^{3+}) = 93.8 pm, both cations are 6-fold coordinated) [49]. In contrast, the crystallite size was found to decrease with increasing the amount of Gd^{3+} doping, which might be due to the difference between the ionic radius between Ti^{4+} and Gd^{3+} which induces a perturbation in anatase crystal structure and inhibits the crystallites growth [50]. As the ionic radius of Gd^{3+} is about 1.5 times bigger than that of Ti^{4+}, it tends to exist at the interstices or crystal boundaries, most probably through the Ti—O—Gd structure which restricts the direct connection between crystallites and inhibits the crystal growth [50,51]. Moreover, Gd^{3+} resides in the octahedral interstitial site for TiO$_2$ with the

high oxygen affinities, where it creates localized positive charge around titanium or form an oxygen vacancy [52]. The amount of oxygen vacancies formed for compensating the charge difference between Ti^{4+} and Gd^{3+} are expected to be increased with increasing the amount of Gd^{3+} doping in the TiO_2 lattice. This finding has been further confirmed by Raman and XPS analyses as discussed below. As shown in Table 1, all samples exhibit high microstrain, which may be due to their lattice distortion and nanosized crystallites.
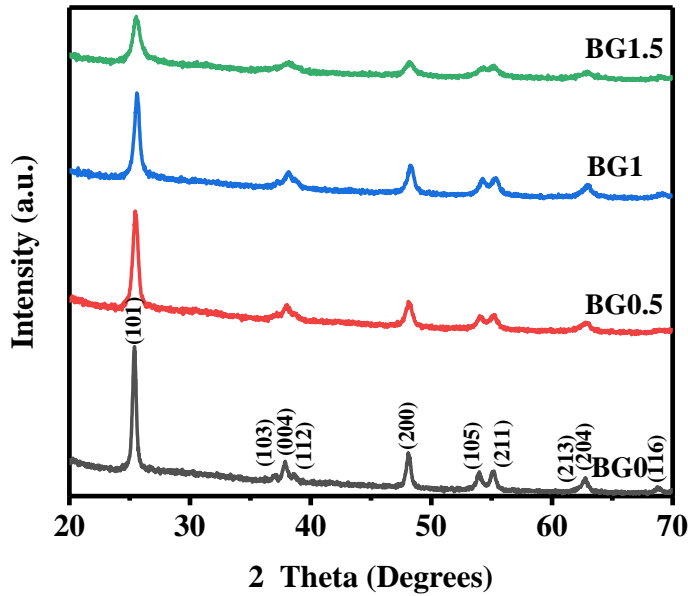

Figure 1. XRD patterns of all the elaborated nanofibers: BG0, BG0.5, BG1 and BG1.5

Table 1. Calculation of lattice parameters, unit cell volume, crystallites size and microstrain from XRD

Sample	Lattice parameter (Å)	Unit cell volume (Å³)	crystallites size (nm)	Micro-strain x 10⁻³
BG0	3.7912±0.0004	136.92±0.03	31.7±0.3	3.55±0.02

	9.526±0.001			
BG0.5	3.7939±0.0007 9.516±0.001	136.97±0.05	16.9±0.4	4.80±0.03
BG1	3.7961±0.0005 9.517±0.001	137.14±0.03	13.9±0.6	3.42±0.05
BG1.5	3.7978±0.0009 9.516±0.002	137.25±0.07	8.7±0.7	3.67±0.04

The morphology of nanofibers was analysed using SEM and TEM microscopy as shown in Figure (2 a-h) and Figure (S2), respectively. The average diameter of the nanofibers was decreased from ~ 0.35(3) µm for BG0 sample to 0.25(4) µm for BG1.5 sample. This reduction in the diameter of the nanofiber with increasing the amount of Gadolinium indicates the successful incorporation of gadolinium into nanofibers. This result is in good agreement with XRD results which revealed similar decrease in crystallite size with increasing the amount of Gd^{3+} doping. In order to confirm the doping of gadolinium into TiO_2 lattice, some of the nanofibers were further analysed by HRTEM. The tetragonal structure of TiO_2 in the samples BG0 and BG1.5 was confirmed with the measured of interplanar spacings of 0.297 nm and 0.305 nm, respectively, corresponding to the (101) plane (Figure 2 i and j, t). The larger d_{101} spacing of TiO_2 in BG1.5 in comparison with that in BG0 indicates the expansion in the unit cell volume due to the incorporation of Gd^{3+} ions in TiO_2 lattice. This result is in agreement with our XRD analysis and previously reported works [53]. The SAED pattern of BG0 and BG1.5 are demonstrated in inset of Figure (2 i and j), the crystallinity changed from pure anatase to a polycrystalline structure by the incorporation of gadolinium.

Furthermore, the energy dispersive X-ray (EDX, Table S1) analysis on several nanofibers in each sample confirms the incorporation of Gd^{3+} into the TiO_2 nanofibers. The increase of atomic ratio of Gd^{3+}/Ti^{4+} in BG1.5 > BG1 > BG0.5 can be clearly seen from Table S1, which is in consistent with the experimental values. The Elemental mapping image (Figure S3) shows that the distribution of Gd^{3+}, BN and TiO_2 in BG1.5 sample is homogenous and uniform. Based on these data, the $BN/Gd_xTi_{(1-x)}O_{(4-x)/2}$ nanofibers have been proved to be successfully elaborated by the electrospinning method.

The reduction in the crystallite size and the diameter of the prepared nanofibers with Gd doping was further confirmed by BET measurements. When the size of the crystallite decreases the surface area is expected to increase. In consistent with XRD and TEM results, BET results showed that S_{BET} of BG0, BG0.5, BG1 and BG1.5 are 12, 15, 41 and 58 m^2g^{-1}, respectively, which suggests a decrease in the size of the crystallite and/or the nanofibers with increasing Gd doping. It worth noting that the enhancement of surface area is a key factor to improve photocatalytic activity [10]. Larger specific surface area of BG1.5 could allow rapid diffusion of reactants and products and thus enhancing the photocatalytic reaction.
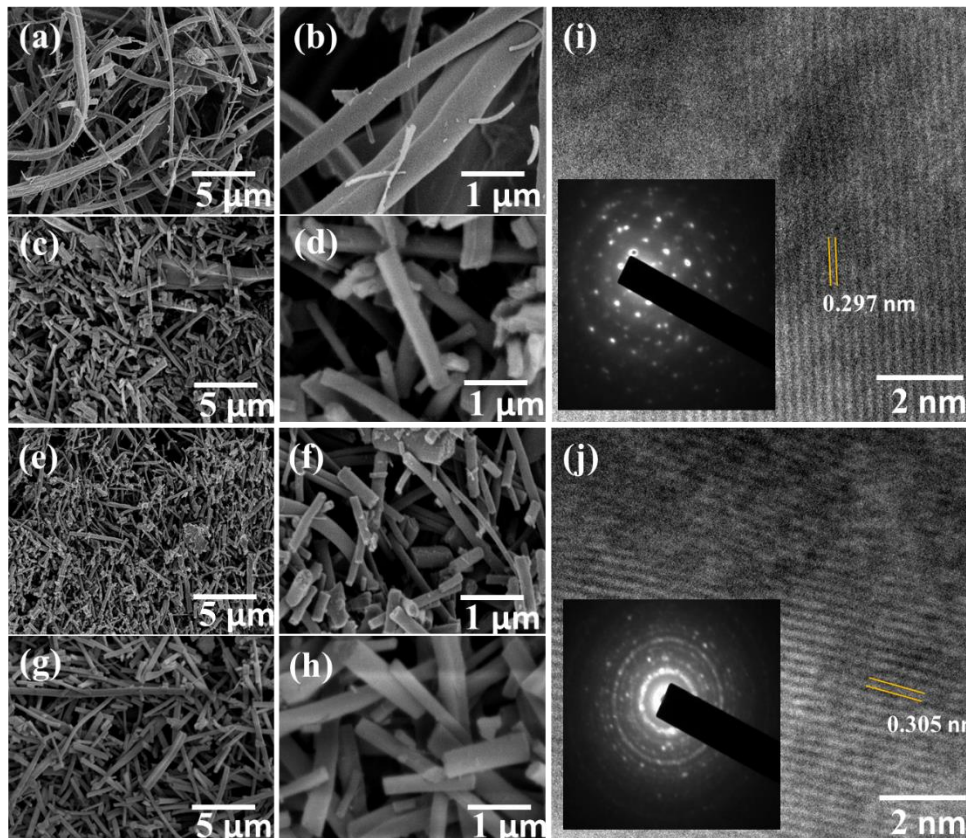
Figure 2. Scanning electron microscope images of BG0 (a and b), BG0.5 (c and d), BG1 (e and f) and BG1.5 (g and h), high-resolution transition microscope of BG0 (i) and BG1.5 (j) and the SAED pattern of BG0 in inset (i) and BG1.5 in inset (j).

In the next step, the effect of Gd^{3+} doping on the crystal structure of anatase TiO_2 was studied by Raman and FTIR spectroscopies. According to group theory, the tetragonal structure of anatase TiO_2 (space group $I4_1/amd$) has four formula units per unit cell and possesses six Raman active modes (A1g + 2B1g + 3Eg), three infrared active modes (A2u + 2Eu) and one vibration of B2u which is inactive in either the infrared or Raman spectra [54,55]. As shown in Figure 3 a and b, these six active Raman modes are observed at 143.8 (E_g), 196.5 (E_g), 395.5

(B_{1g}), 513 (A_{1g}), 519 (B_{1g}) and 637.5 (E_g) cm^{-1} in all samples suggesting the formation of TiO_2 anatase phase, which is consistent with the XRD analysis.

The Raman mode observed at 1367 cm^{-1} can be assigned to the vibration mode E_{2g} that is characteristic of hexagonal BN [28]. The additional Raman bands observed at 247.5, 318 and 364 cm^{-1} in spectra of BG1 and BG1.5 samples can be ascribed to brookite structure [56]. However, the amount of brookite phase is assumed to be very small as it was not detected in the XRD measurements (Figure 1). This result indicates an increase in the distortion of anatase lattice with the increase of Gd^{3+} doping, which results in the formation of brookite with distorted orthorhombic structure (space group *Pbca*). Moreover, the broadening and the shift of the Raman bands, in particular the E_g mode near 143.8 cm^{-1}, towards higher wavenumbers with increasing the Gd^{3+} amount can be attributed to either the reduction of the crystallite size or the expansion/distortion of TiO_2 lattice as shown in Figure (S4) [57]. In addition, these broadening and shifting in wavenumbers can be explained by enriched of oxygen vacancies [58–60]. It is well known that the vibrational modes of materials are greatly affected by the crystallite size (Heisenberg uncertainty principle) [61]. As the size of crystallites decreases to the nanoscale, the surface stress produces an effective pressure that leads to rise of the force constants. Therefore, the Raman bands shifted to higher wavenumber, where it varies in proportion to root of force constant [61]. The observed frequencies for E_g mode of our samples are very close to those simulated and measured due to small size-effect in nanocrystalline anatase TiO_2 [62], suggesting that the phonon confinement is the main mechanism responsible for the shift of the Raman bands towards higher wavenumbers, and the lattice expansion/distortion has only a little influence on this shift. Moreover, very small influence on the frequency of E_g mode was observed for Gd

doped TiO_2 specimens; those have very close crystallite size despite the large difference in their unit cell volume [63].

The successful incorporation of BN nanosheets in TiO_2 nanofibers was further confirmed by FTIR spectroscopy. As displayed in Figure S5, the main absorption band attributed to the B-N bonding in *h*-BN was observed around 1386 cm^{-1} [64], while the absorption band located at 650–900 cm^{-1} can be assigned to Ti–O bonding in TiO_2 nanofibers [28]. The small absorption bands observed at 2800-2900 cm^{-1} in the spectra of gadolinium samples can be assigned to C-H bond, which suggests the presence of small amount of organic residue from the organic precursors used in the experiments.
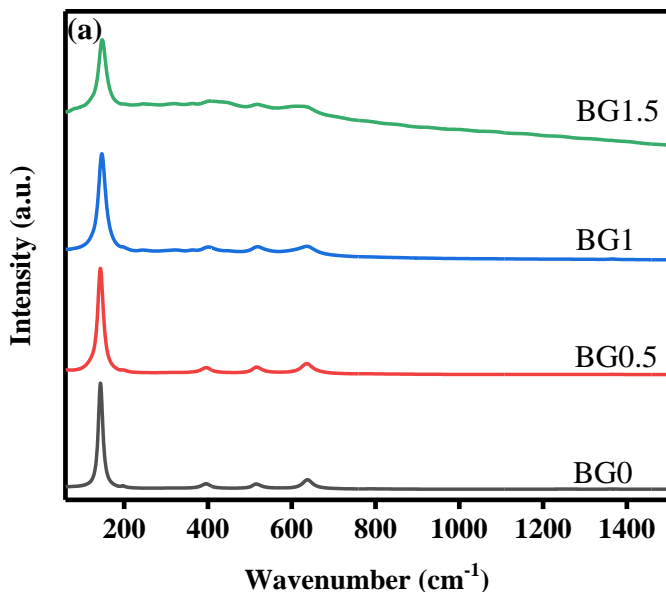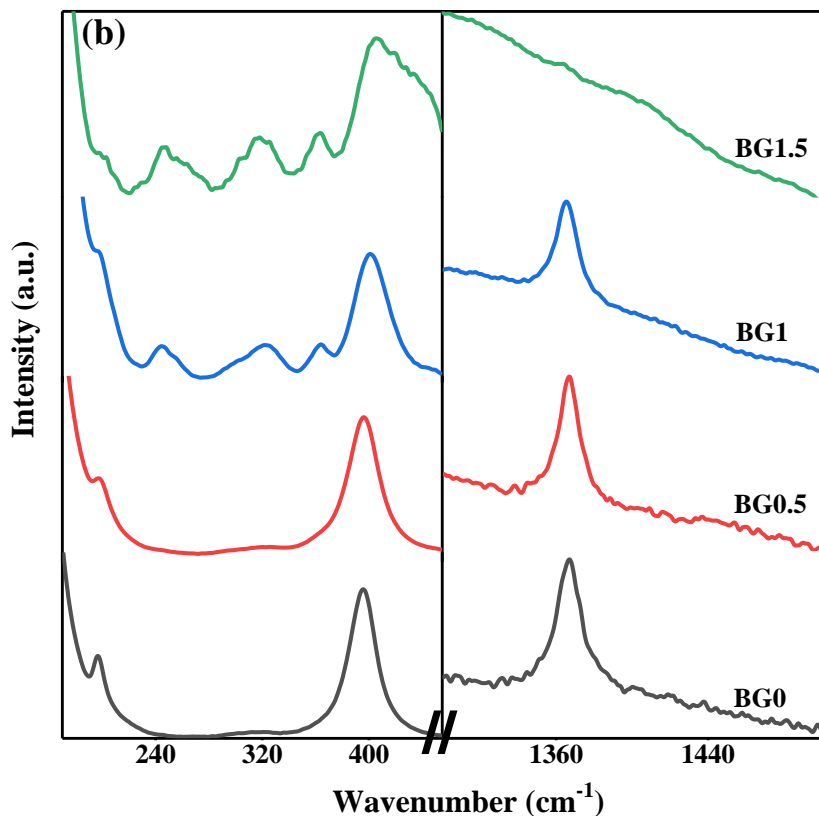
Figure 3. Raman spectra of all prepared nanofibers BG0, BG0.5, BG1 and BG1.5 on the wavenumber range of 60−1500 cm^{-1} (a) and on the wavenumber range of 170−455 cm^{-1} incorporated with the wavenumber range of 1300-1500 cm^{-1} (b).

Further insights into the effects of Gd^{3+} doping on the chemical composition and chemical states on the surface of the prepared nanofibers were obtained by using X-ray photoelectron spectroscopy analysis (XPS). Figure S6 shows XPS survey spectra of undoped BG0 sample as well as the Gd^{3+} doped BG1 and BG1.5 samples. The high resolution XPS spectra of O 1s, Ti 2p, Gd 4d and N 1s orbitals are displayed in Figure 4 a-d. As shown in Figure 4a, the O 1s spectrum can be fitted with two peaks at ~530 and 531.4 eV corresponding to the lattice oxygen (O_{latt}) and the surface adsorbed oxygen ($O_{ads.}$), respectively [65]. The ratios of O_{ads}/O_{latt} can refer to the

amount of surface oxygen vacancies. The higher ratio suggests a larger amount of surface oxygen vacancies. As shown in Table 2, the ratios of O_{ads}/O_{latt} were found to be 0.415 and 0.336 in the BG1.5 and BG1 samples, which are higher than that in undoped BG0 sample (0.233). The high amount of oxygen vacancies generated in the BG1 and BG1.5 samples is due to the substitutions of Ti^{+4} by Gd^{3+} in TiO_2 lattice as the charge compensation of oxygen as negative part against positive part (Ti^{+4} and Gd^{3+}) in the lattice [1,66]. Similarly, the XPS of Ti2p core (Figure 4b) can be fitted with two peaks at about 458.9 and 464.6 eV, which attributed to the Ti $2p_{1/2}$ and Ti $2p_{3/2}$, respectively, arise from the spin orbit-splitting. These two peaks ensure the characteristic binding energies of Ti^{4+} in the TiO_2 matrix [67]. The Ti 2p peaks are shifted to lower binding energies by about ~0.2 eV for BG1.5 sample, which suggests the doping of Gd^{3+} ions in the TiO_2 lattice. The Pauling electronegativity value of Ti (1.5) is more than Gd (1.2) so a charge transfer from Gd^{3+} to Ti^{4+} through Ti-O-Gd bond is expected. This leads to an increase in the electron surrounding the Ti atoms [1] and thus Ti 2p of Ti is shifted to lower binding energy. Moreover, the incorporation of Gd^{3+} ions in the TiO_2 lattice was confirmed by recording the XPS spectrum of Gd 4d core of BG1 and BG1.5 samples. As shown in Figure 4c, two peaks are observed at about 142.5 and 147.4 that can be assigned to the the Gd $4d_{5/2}$ and Gd $4d_{3/2}$, respectively. These two peaks are observed at higher binding energy by about 1.1 eV in the pure Gd_2O_3 [1], which confirms the presence of Gd^{3+} ions in TiO_2 lattice. As discussed above, the charge transfer from Gd^{3+} to Ti^{4+} ions through Ti-O-Gd bonds results in an increase in the electron density of Ti ions, while, a decrease in the electron density of Gd ions is expected. Therefore, the XPS peaks corresponding to Ti ions shifted to lower binding energies, while, those corresponding to Gd ions are shifted to higher binding energies in comparison with those in pure TiO_2 and Gd_2O_3 oxides, respectively. As shown in Table 2, the Gd/Ti mole ratios

measured from XPS spectra are 0.016 and 0.034% in the surface of BG1 and BG1.5 samples, respectively. These values are very close of those determined by EDX analysis, where Gd/Ti mole ratios were 0.022 and 0.030 in BG1 and BG1.5, respectively. Moreover, as shown in Table 2, the decrease of the O_{latt}/Ti and O_{latt}/(Ti+Gd) mole ratios with increasing the Gd/Ti mole ratio in the doped samples, confirms the high amount of oxygen vacancies generated on the surface of BG1 and BG1.5 samples due to the substitutions of Ti^{+4} by Gd^{3+} in TiO_2 lattice as the charge compensation of oxygen as negative part against positive part in the lattice [68,69]. Finally, the presence of BN in the nanofibers was confirmed by observing a peak at ~398.3-397.9 eV in the N 1s spectrum of all samples (Figure 4d). This peak is usually observed at about 398.3 eV in the N 1s spectrum for h-BN [70]. However, the shift in the position of this peak to lower binding with increasing the amount of Gd amounts may indicate the presence of interactions between the Gd doped TiO_2 nanofibers and the BN nanosheets [1].
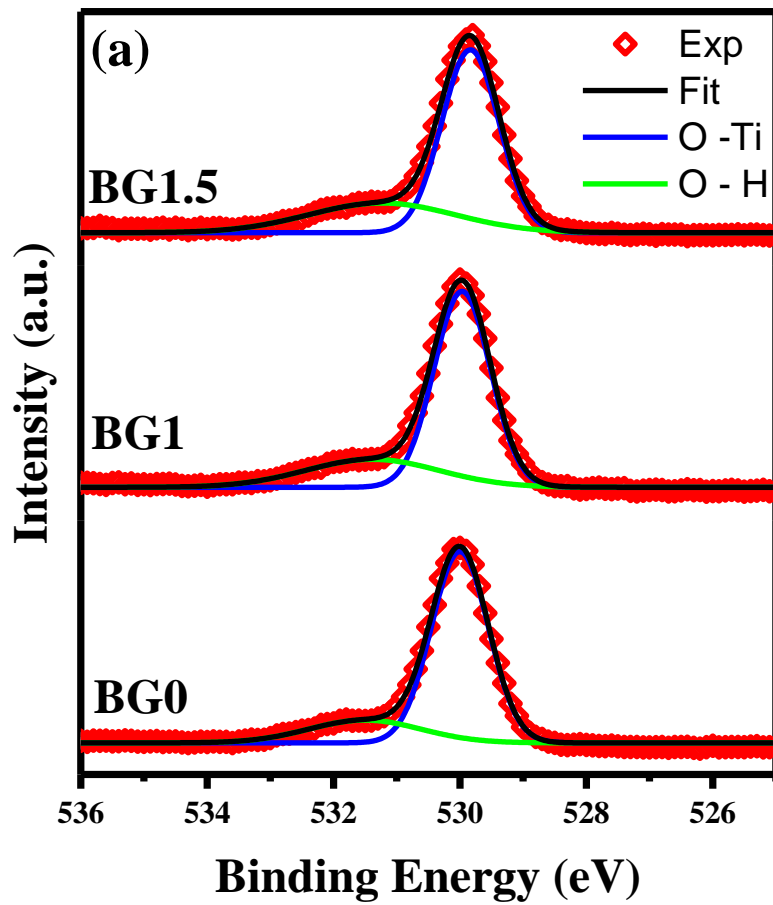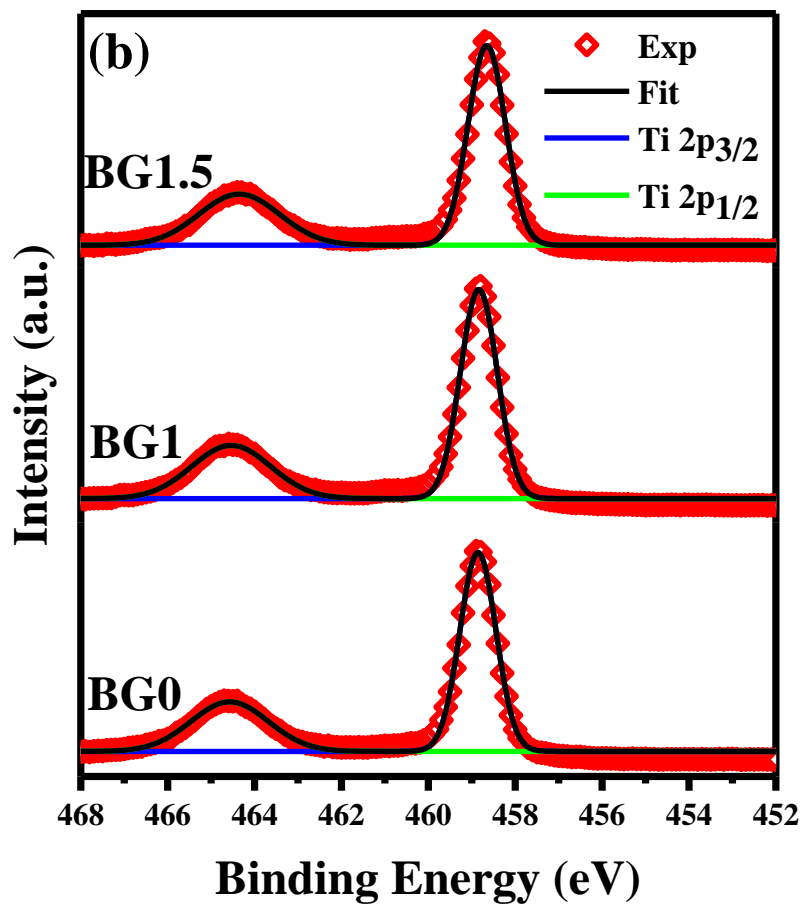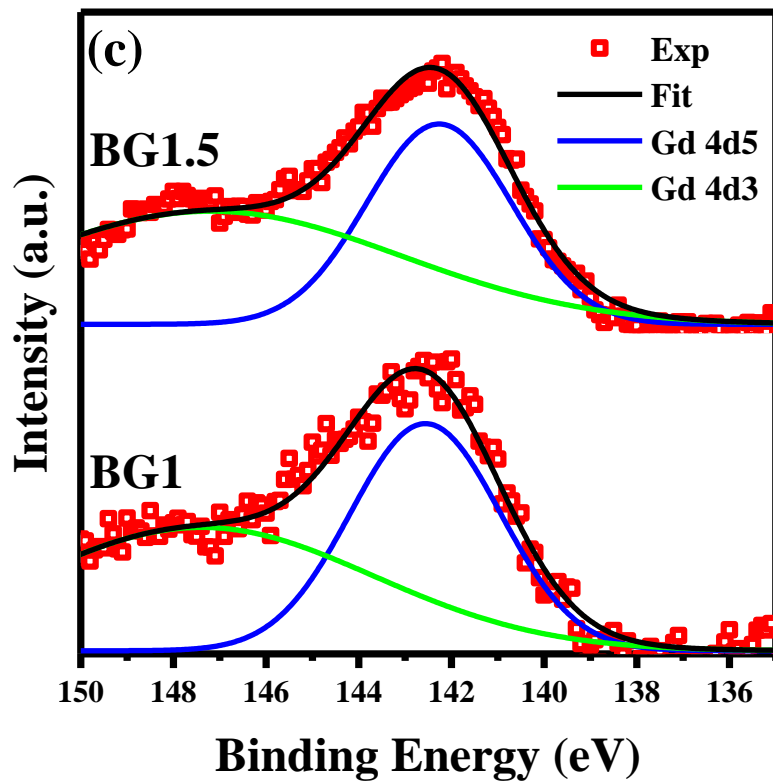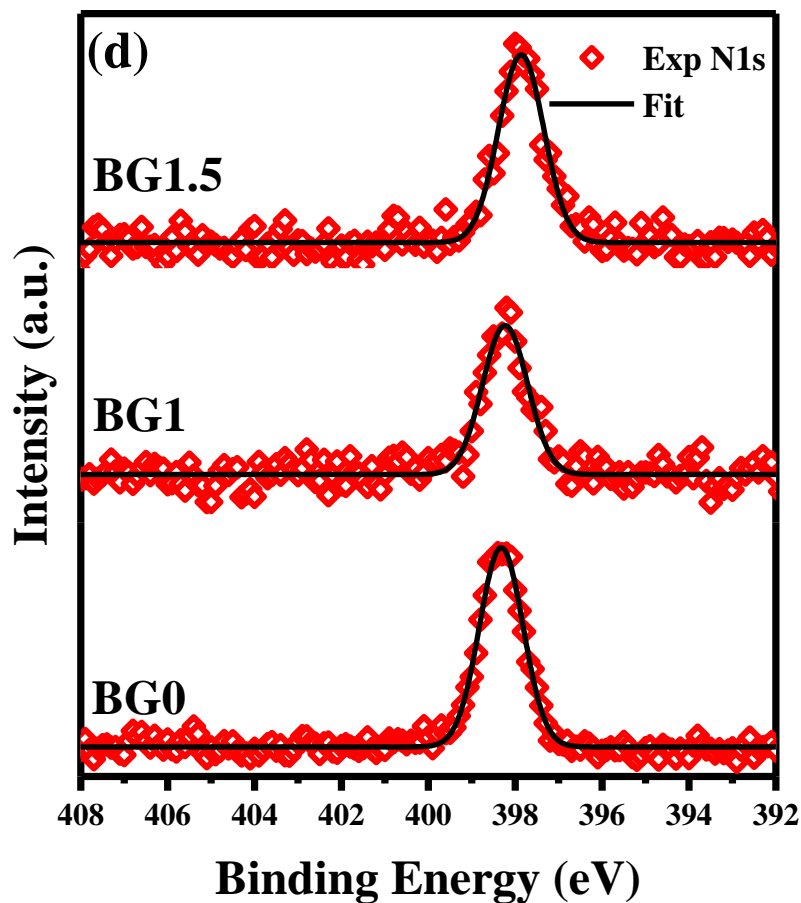
Figure 4. High-resolution XPS spectra of O1s (a), Ti2p (b), N1s (c) and Gd4d for G0, G1 and G1.5 nanofibers.

Table 2. The O_{latt}/Ti, O_{latt}/(Ti+Gd), Gd/Ti and O_{ads}/O_{latt} ratios on the surface of the samples calculated from XPS analysis.

	BG0	BG1	BG1.5
O_{latt}/Ti	1.855	1.744	1.661
O_{latt}/(Ti+Gd)	1.855	1.717	1.606
Gd/Ti	0	0.016	0.034
O_{ads}/O_{latt}	0.233	0.336	0.415

In the next step, the influence of Gd^{3+} doping on the optical band gap of the prepared TiO_2 nanofibers will be investigated by UV-Vis absorbance measurements as shown in Figure (5). The

optical band gap E_g of the samples was determined by Kubelka-Munk remission function according to the following equation [13]:

$$\alpha h v = A(hv - Eg)^2 \quad \text{equation (5)}$$

where α is the absorption coefficient, v is light frequency and E_g is indirect transition band gap.

The E_g values of BG0, BG0.5, BG1 and BG1.5 are 3.12, 3.13, 3.20 and 3.22 eV, respectively, which indicates a slight increase in the optical band gap with increasing the Gd content. This blue shift can be explained by the quantum size effect as XRD results showed a decrease in the crystallite size of the nanofibers with the increasing the Gd content [71]. Moreover, recent DFT calculation on Gd doped TiO_2 showed that the impurity energy levels of the 4f, 5d and 6s states presence by Gd^{3+} at the top of valence band of TiO_2, affect the position and width of the valence and the conduction bands [24]. As a result, the optical band gap of TiO_2 could be slightly shifted to higher energy with increasing the amount of Gd^{3+} doping. However, there are new absorption peaks at 2 eV, related to transitions between Vo (oxygen vacancies level) and VC and VB as presented in inset (Figure 5). This led to the increasing of absorption in the visible range, what could be related to the oxygen vacancies. Additionally, the electrons transfer between the 4f state of the Gd^{3+} ions and CB or VB of TiO_2 could shift the photocatalytic activity of TiO_2 from UV to the visible region [66,72]. The defect levels between CB and VB are one of the important strategies to make a semiconductor active under visible light [73,74]. Accordingly, the prepared nanofibers are expected to show a photocatalytic activity in the visible region as it will be discussed below.
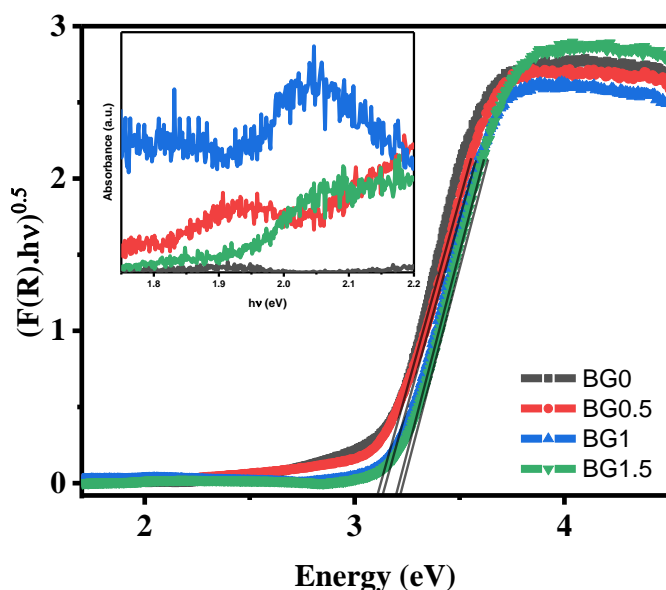
Figure 5. Plot of Transformed Kubelka – Munk function against the energy for BG0, BG0.5, BG1 and BG1.5 samples

The electrochemical impedance spectroscopy analysis was performed to determine the regarding lifetime, separation efficiency and transmission rate of the photo-induced charge carriers. The EIS is a powerful technique for assessment of the charge transfer and recombination processes at the interface of nanofibers and electrolyte. The Nyquist and Bode phase curves of EIS at the open-circuit potential under visible light irradiation for prepared nanofibers are shown in Figure 6 a and b and the proposed equivalent circuit is illustrated in the inset of Figure 6a. The decreasing of the semicircle diameter at Nyquist plot with the increasing of gadolinium doping refers to a lower resistance between fibers and electrolyte interface. This could be attributed to a higher electron transfer induced by the increase of oxygen vacancies concentration. Among the fitted parameters of the equivalent circuit, R_1 is the bulk resistance of electrodes and electrolyte, R_2 represents the resistance formed at the interface of the nanofibers and electrolyte and Q_2

denotes the double layer capacitance at the nanofibers and the electrolyte interface; all these parameters were illustrated in Table 3. BG1.5 has the fastest charge transfer rate and the best photogenerated electron-hole separation than other prepared nanofibers because it exhibits the lowest R_2 (3.5 k.ohm) among all samples. Moreover, the characteristic peak of the nanofibers in bode-phase plot (Figure 6b) is shifted to lower frequency range with increasing the Gd^{3+} doping, which indicates the reduction of recombination rate between electrons and holes and thus longer life time of electrons [75]. The electron life time before recombination was determined from the following equation [50]:

$$t_e = 1/2\pi f_{max} \qquad\qquad \text{equation (6)}$$

where, t_e is an average time before recombination e^-/h^+ and f_{max} is the maximum frequency at the mid frequency peak. The values of f_{max} and t_e for the prepared nanofibers are listed in Table 3. BG1.5 shows the longest lifetime in comparison with the other samples as Gd doping reduces the recombination rate between electrons and holes. Moreover, the presence of 4f orbitals in Gd^{3+} ions could act as traps for promoting the charge transition process.
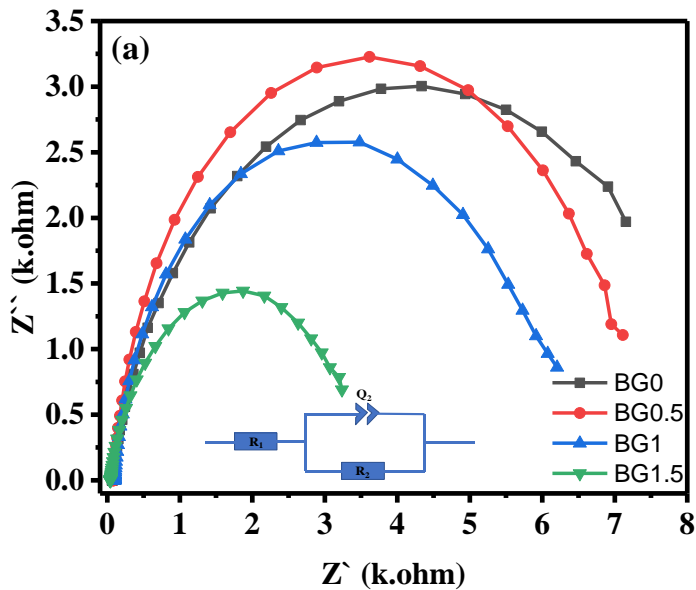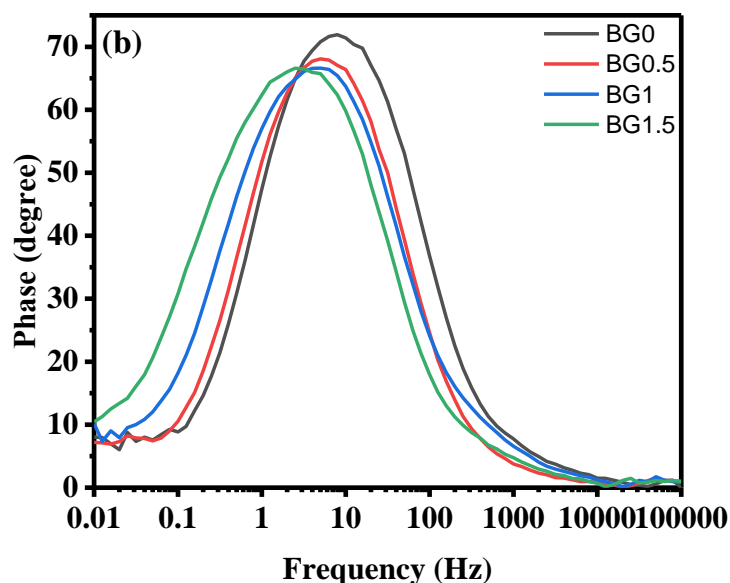
Figure 6. The Nyquist (a) and Bode phase (b) curves of EIS spectra of BG0, BG0.5, BG1 and BG1.5 samples.

Table 3. EIS parameters and life time of electrons in all nanofibers

Sample	R_1 (ohm)	R_2 (K.ohm)	f_{max} (Hz)	t_e (ms)
BG0	73.02	7.73	7.9	20.16
BG0.5	84.52	7.19	5.0	31.85
BG1	99.95	6.03	5.0	31.85
BG1.5	43.77	3.51	2.5	63.69

The photocatalytic activity of the elaborated nanofibers for water splitting is shown in Figure 7(a). It can be observed that the rate of H_2 production under visible light was increased with increasing of gadolinium in the nanofibers. The hydrogen yield reached 6325 µmol/g.h for BG1.5; which presents three hundred times compared with TiO_2-P25; This enhancement could

be ascertained to the stability and the long-life time of electrons and holes as revealed by EIS measurements. Moreover, the electrons transfer between the impurities levels between CB and VB could enhance the photocatalytic activity nanofibers under visible light [72]. In addition, the hydrogen yield in absence of methanol (BG1.5-W) reached 1900 µmol/(g.h). Furthermore, the experiments for the photocatalytic activity of BG1.5 nanofibers were repeated using different loading amounts of the catalyst (1-50 mg). As shown in Figure 7b, the rate of H_2 yield is increased with increasing the amount of BG1.5 nanofibers from 1 to 5 mg. The best hydrogen yield (i.e. 192602 µmole/g) is detected using 5 mg loading amount of the catalyst after a reaction time of 6 hours. A further increase of BG1.5 nanofibers to 50 mg induces a lower rate of hydrogen production. This depression behaviour with high amount of the catalyst can be due to the limit in the absorption of incident light by the agglomerated catalyst [1]. Herein, 5 mg BG1.5 nanofibers is found to be the optimum amount of photocatalyst for extreme rate of hydrogen production.
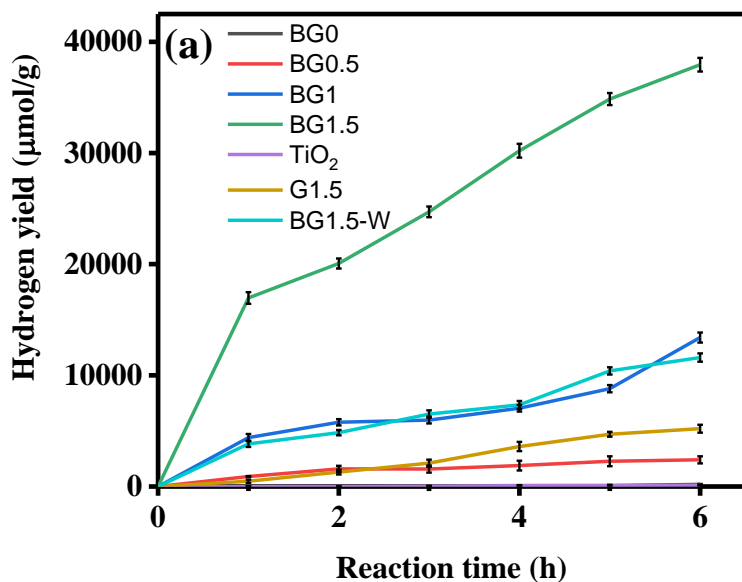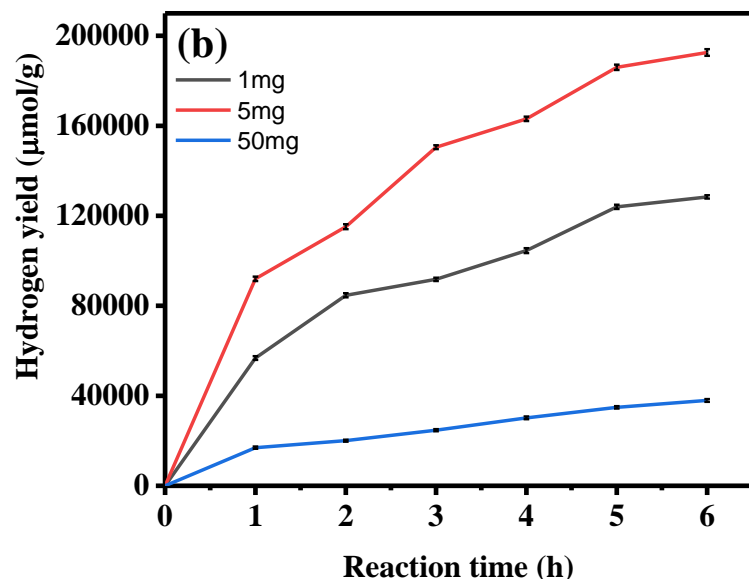
Figure 7. Effect of Gd and BN on the photocatalytic hydrogen production under visible light (a) and effect of BG1.5 catalyst amount on the photocatalytic H_2 production under visible light (b).

To evaluate the durability of the BG1.5 sample, the photocatalytic experiments were performed in four cycles where each cycle lasts for 6 h as shown in Figure 8. It can be seen that the production of hydrogen was linear up to 5 h and then found to be semi-stable. This may be due to the occupation of the surface of photocatalyst by some H_2 which could hinder the production of hydrogen. The capacity of the photo-reactor may also become unsuitable for producing more hydrogen [76,77]. We can note also that the crystallinity of BG1.5 nanofibers (Figure S7) and the composition (Table S1) were stable after four cycles as confirmed by XRD and EDX respectively. Table 4 represents the maximum photocatalytic activity of various gadolinium/TiO_2 photocatalysts for hydrogen production demonstrating the outstanding performance of our $BN/Gd_xTi_{(1-x)}O_{(4-x)/2}$ nanofibers.
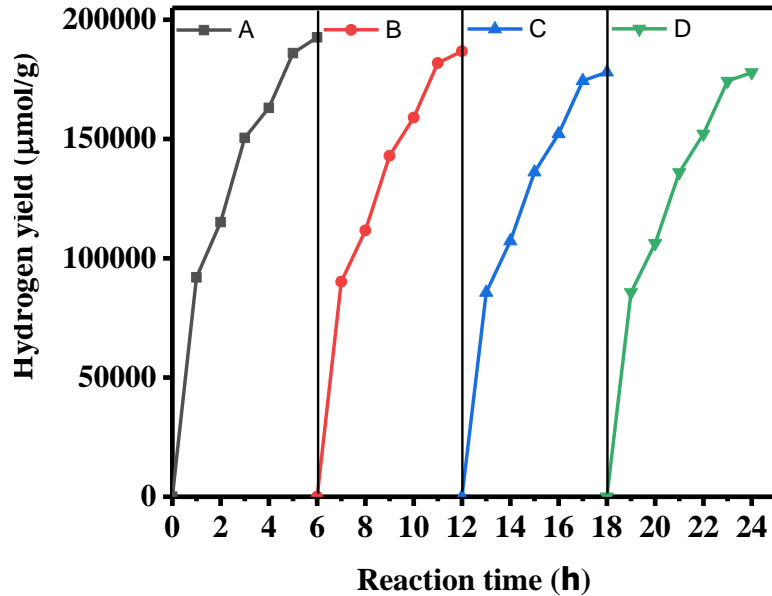
Figure 8. Reusability of BG1.5 nanofibers for photocatalytic H_2 production activity under visible light.

Table 4. Maximum photocatalytic activity of various gadolinium/TiO_2 photocatalysts.

Photocatalysts	The light source	Sacrificial agent	H_2 evolution Rate ($\mu mol/h.g$)	Q.E.	Ref.
$TiO_2/Gd_2O_3/Pt$	Ultra-Vitalux lamps 300 W (as the natural solar irradiation)	2 vol.% Methanol	13775	---	[34]
$Gd_2Ti_2O_7$	High-pressure mercury lamp 400 W	Water	800	---	[33]
$Gd_2Ti_2O_7/GdCrO_3$	Medium pressure Hg lamp 125 W (as visible light source)	10 vol.% Methanol	12555	4.1	[36]
2wt.% Gd and N co-doped TiO_2	Natural solar irradiation	5 vol.% Methanol	1076	---	[1]
TiO_2-1wt.% Pt	Photo-CREC Water II Reactor with black light blue lamp	2 vol.% Ethanol	$383*10^6$	7.9	[78]

P25-5Pt	Hg-Xe lamp (500 W).	50 vol.% Methanol	27600	28	[79]
2.5 wt.% Pt/Meso-TiO$_2$	Photo-CREC Water II Reactor with black light blue lamp	2 vol.% Ethanol	669	22.6	[80]
3Ru/TiO$_2$	500W Xe lamp (UV light: 280–400 nm)	30 vol.% Methanol	4600	3.1	[44]
BG1.5	Linear halogen lamp 500 W (visible light source)	20 vol.% Methanol	6324	8.8	This work
		Water	1933	2.7	This work

The total hydrogen production over semiconductor photocatalyst is mainly determined by the capacity of adsorption reactants and desorption product as well as the amount of excited electrons in the water/photocatalyst interface [1,10]. Therefore, the good specific surface area and high oxygen vacancies on the surface of the samples are beneficial for adsorption/desorption process, which possess sufficient reactive sites to enhance their photocatalytic efficiency. Additionally, the 1D geometry of the nanofiber could reduce the aggregation of the photocatalysts, which increases the time of their applications. Moreover, the presence of 2D-BN structure enriched the adsorption/desorption process for improved hydrogen yield [81]. According to the results discussed above, the mechanism of hydrogen production using BN/Gd$_x$Ti$_{(1-x)}$O$_{(4-x)/2}$ nanofibers can be explained as follows (Figure 9). From XRD, Raman and XPS, we can conclude that the oxygen vacancies states were above the valence band. Density functional theory (DFT) calculations of Gd^{3+}/TiO$_2$ showed impurity energy levels such as 4f, 5d, and 6s states above the valence band of TiO$_2$ [82,83]. When the nanofibers are excited with visible light, the electron and holes are generated to react with water solutions. The excited

electrons from valence band can be trapped by the impurity states. Then these electrons can reach the conduction band by absorbing the low energy photons. Hence, the conduction band accepted more electrons under visible light. The hydrogen was produced from electrons with protons. In another hand, the holes were scavenged rapidly by h-BN nanosheets due to the electrostatic attraction between the positive charge of holes and the negative charge of BN [84,85]. In addition, the BN on the surface of the TiO_2 contributed to the enhancement of the separation of e-/h$^+$ and the extension of the lifetime of photo-excitons. This led to the outstanding performance of our nanofibers for the hydrogen production. Our finding is in line with a recently proposed mechanism for the photoctalytic H_2 production activity over 2wt.% Gd and N co-doped TiO_2 catalyst under natural and stimulated sunlight irradiation [1]. As their photocatalyst do not contain BN nanosheet, they used methanol in their photocatalytic experiment to scavenge the holes and thus decrease the recombination of electron and hole. As it can be seen from Figure 7a and Table 4, BG1.5 sample shows much better photocatalytic H_2 production activity without using methanol in comparison with that of 2wt.% Gd and N co-doped TiO_2 even with using methanol sacrificial agent, confirming the important role of BN in the separation of e$^-$/h$^+$ and the extension of the lifetime of photo-excitons. However, the using of methanol could lead to additional reduction of the e$^-$/h$^+$ recombination process. Methanol is added to a water mixture as donor-like material [86]. Therefore, BG1.5 sample in the presence of methanol exhibits outstanding photocatalytic activity.
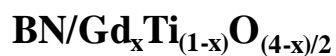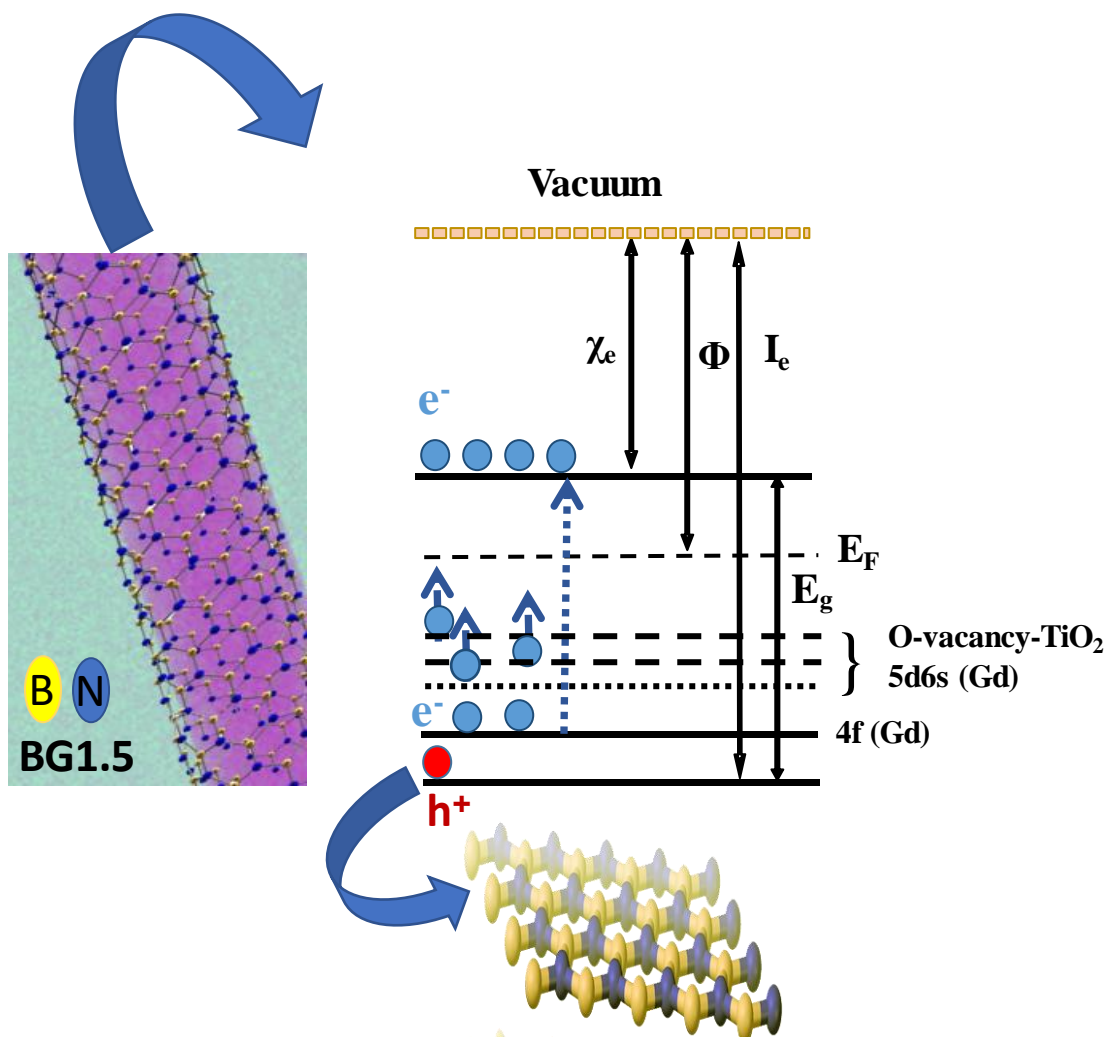
Figure 9. Schematic representation of excitations in BG1.5 under visible light.

CONCLUSIONS

This unprecedented study investigated $BN/Gd_xTi_{(1-x)}O_{(4-x)/2}$ nanofibers as novel photocatalyst for hydrogen production by water splitting under visible light. The formation of oxygen vacancies and defect levels in the TiO_2 structure lead to the extent of the TiO_2 absorption into visible region. The presence of BN together with impurity levels improved the life time of electrons and holes. The electrochemical impedance spectroscopy study confirmed that these defects sites are

playing indispensable role in improving the charge carrier transfer and separation in nanofibers. BG1.5 nanofibers (1.5 mol% of gadolinium) demonstrated outstanding hydrogen production performance by water splitting under visible light, thousand times higher than that of pristine nanofibers without gadolinium and 7 times higher than nanofibers without BN. The hydrogen production reached up to 192602 ± 1500 µmole/g during 6 hours under visible light. The synergistic effect between Gd^{3+} and BN in TiO_2 nanofibers, which had not been reported yet, could not only enabled to enhance the absorption in visible region but also enabled to reduce the recombination time between electrons and holes.

ACKNOWLEDGMENTS

REFERENCE

[1]   K.K. Mandari, A.K.R. Police, J.Y. Do, M. Kang, C. Byon, Rare earth metal Gd influenced defect sites in N doped TiO_2: Defect mediated improved charge transfer for enhanced photocatalytic hydrogen production, Int. J. Hydrogen Energy. 43 (2018) 2073–2082. doi:10.1016/j.ijhydene.2017.12.050.

[2]   K. Chung, S. Jeong, B. Kim, K. An, Y. Park, S. Jung, Enhancement of photocatalytic hydrogen production by liquid phase plasma irradiation on metal-loaded TiO_2/carbon nanofiber photocatalysts, Int. J. Hydrogen Energy. 43 (2018) 11422–11429. doi:10.1016/j.ijhydene.2018.03.190.

[3]   M. Cheng, G. Zeng, D. Huang, C. Lai, P. Xu, C. Zhang, Y. Liu, J. Wan, X. Gong, Y. Zhu,

Degradation of atrazine by a novel Fenton-like process and assessment the influence on the treated soil, J. Hazard. Mater. 312 (2016) 184–191. doi:10.1016/j.jhazmat.2016.03.033.

[4]   C. Zhou, C. Lai, D. Huang, G. Zeng, C. Zhang, Highly porous carbon nitride by supramolecular preassembly of monomers for photocatalytic removal of sulfamethazine under visible light driven, Appl. Catal. B Environ. 220 (2018) 202–210. doi:10.1016/j.apcatb.2017.08.055.

[5]   C. Zhou, C. Lai, P. Xu, G. Zeng, D. Huang, C. Zhang, M. Cheng, L. Hu, J. Wan, Y. Liu, W. Xiong, Y. Deng, M. Wen, In Situ Grown AgI/$Bi_{12}O_{17}Cl_2$ Heterojunction Photocatalysts for Visible Light Degradation of Sulfamethazine: Efficiency, Pathway, and Mechanism, ACS Sustain. Chem. Eng. 6 (2018) 4174–4184. doi:10.1021/acssuschemeng.7b04584.

[6]   C. Zhou, C. Lai, P. Xu, G. Zeng, D. Huang, Z. Li, C. Zhang, Rational Design of Carbon-Doped Carbon Nitride/$Bi_{12}O_{17}Cl_2$ Composites: A Promising Candidate Photocatalyst for Boosting Visible-Light-Driven Photocatalytic Degradation of Tetracycline, ACS Sustain. Chem. Eng. 6 (2018) 6941–6949. doi:10.1021/acssuschemeng.8b00782.

[7]   R. Li, Latest progress in hydrogen production from solar water splitting via photocatalysis , photoelectrochemical , and photovoltaic - photoelectrochemical solutions, Chinese J. Catal. 38 (2017) 5–12. doi:10.1016/S1872-2067(16)62552-4.

[8]   P. Wu, Z. Liu, D. Chen, M. Zhou, J. Wei, Flake-like NiO/WO_3 p-n heterojunction photocathode for photoelectrochemical water splitting, Appl. Surf. Sci. 440 (2018) 1101–1106. doi:10.1016/j.apsusc.2018.01.292.

[9]   T. Wang, Y. Wei, X. Chang, C. Li, A. Li, S. Liu, J. Zhang, J. Gong, Homogeneous Cu_2O

p-n junction photocathodes for solar water splitting, Appl. Catal. B Environ. 226 (2018) 31–37. doi:10.1016/j.apcatb.2017.12.022.

[10]   H.H. El-maghrabi, A. Barhoum, A.A. Nada, Y. Mohamed, S. Mikhail, A.M. Youssef, Synthesis of mesoporous core-shell CdS@TiO2 (0D and 1D) photocatalysts for solar-driven hydrogen fuel production, "Journal Photochem. Photobiol. A Chem. 351 (2018) 261–270. doi:10.1016/j.jphotochem.2017.10.048.

[11]   H.H. El-maghrabi, E. Ahmed, F.S. Soliman, Y. Mohamed, A.E. Amin, One pot environmental friendly nanocomposite synthesis of novel TiO_2 -nanotubes on graphene sheets as effective photocatalyst, Egypt. J. Pet. 25 (2016) 575–584. doi:10.1016/j.ejpe.2015.12.004.

[12]   M.G. Mali, S. An, M. Liou, S.S. Al-Deyab, S.S. Yoon, Photoelectrochemical solar water splitting using electrospun TiO_2 nanofibers, Appl. Surf. Sci. 328 (2015) 109–114. doi:10.1016/j.apsusc.2014.12.022.

[13]   A.A. Nada, M. Nasr, R. Viter, P. Miele, M. Bechelany, Mesoporous $ZnFe_2O_4$@TiO_2 nanofibers prepared by electrospinning coupled to PECVD as highly performing photocatalytic materials, J. Phys. Chem. C. 121 (2017) 24669–24677. doi:10.1021/acs.jpcc.7b08567.

[14]   M. Nasr, C. Eid, R. Habchi, P. Miele, M. Bechelany, Recent Progress on Titanium Dioxide Nanomaterials for Photocatalytic Applications, ChemSusChem. 11 (2018) 3023–3047. doi:10.1002/cssc.201800874.

[15]   M.A. Kanjwal, W.W.F. Leung, I.S. Chronakis, Composite nanofibers/water photosplitting and photocatalytic degradation of dairy effluent, Sep. Purif. Technol. 192 (2018) 160–165. doi:10.1016/j.seppur.2017.10.015.

[16] T. Lavanya, K. Satheesh, M. Dutta, N. Victor Jaya, N. Fukata, Superior photocatalytic performance of reduced graphene oxide wrapped electrospun anatase mesoporous TiO_2 nanofibers, J. Alloys Compd. 615 (2014) 643–650. doi:10.1016/j.jallcom.2014.05.088.

[17] T. Lavanya, M. Dutta, K. Satheesh, Graphene wrapped porous tubular rutile TiO_2 nanofibers with superior interfacial contact for highly efficient photocatalytic performance for water treatment, Sep. Purif. Technol. 168 (2016) 284–293. doi:10.1016/j.seppur.2016.05.059.

[18] B. Bharti, S. Kumar, H.N. Lee, R. Kumar, Formation of oxygen vacancies and Ti^{3+} state in TiO_2 thin film and enhanced optical properties by air plasma treatment, Sci. Rep. 6 (2016) 1–12. doi:10.1038/srep32355.

[19] J. Lynch, C. Giannini, J.K. Cooper, A. Loiudice, I.D. Sharp, R. Buonsanti, Substitutional or interstitial site selective nitrogen doping in TiO_2 nanostructures, J. Phys. Chem. C. 119 (2015) 7443–7452. doi:10.1021/jp512775s.

[20] M. Zalas, M. Klein, The influence of titania electrode modification with lanthanide ions containing thin layer on the performance of dye-sensitized solar cells, Int. J. Photoenergy. 2012 (2012). doi:10.1155/2012/927407.

[21] M. Zalas, M. Walkowiak, G. Schroeder, Increase in efficiency of dye-sensitized solar cells by porous TiO_2 layer modification with gadolinium-containing thin layer, J. Rare Earths. 29 (2011) 783–786. doi:10.1016/S1002-0721(10)60542-X.

[22] M. Zalas, Gadolinium-modified titanium oxide materials for photoenergy applications: A review, J. Rare Earths. 32 (2014) 487–495. doi:10.1016/S1002-0721(14)60097-1.

[23] M. Nasr, S. Balme, C. Eid, R. Habchi, P. Miele, M. Bechelany, Enhanced visible-light photocatalytic performance of electrospun rGO/TiO_2 composite nanofibers, J. Phys.

Chem. C. 121 (2017) 261–269. doi:10.1021/acs.jpcc.6b08840.

[24]   A. Popa, M. Stefan, D. Toloman, O. Pana, A. Mesaros, C. Leostean, S. Macavei, O. Marincas, R. Suciu, L. Barbu-Tudoran, Fe_3O_4-TiO_2: Gd nanoparticles with enhanced photocatalytic activity and magnetic recyclability, Powder Technol. 325 (2018) 441–451. doi:10.1016/j.powtec.2017.11.049.

[25]   M. Nasr, L. Soussan, R. Viter, C. Eid, R. Habchi, P. Miele, M. Bechelany, High photodegradation and antibacterial activity of BN-Ag/TiO_2 composite nanofibers under visible light, New J. Chem. 42 (2018) 1250–1259. doi:10.1039/c7nj03183a.

[26]   M. Wang, X. Xu, L. Lin, D. He, Gd-La codoped TiO_2 nanoparticles as solar photocatalysts, Prog. Nat. Sci. Mater. Int. 25 (2015) 6–11. doi:10.1016/j.pnsc.2015.01.002.

[27]   B. Singh, G. Kaur, P. Singh, K. Singh, J. Sharma, M. Kumar, R. Bala, R. Meena, S.K. Sharma, A. Kumar, Nanostructured BN-TiO_2 composite with ultra-high photocatalytic activity, New J. Chem. 41 (2017) 11640–11646. doi:10.1039/c7nj02509b.

[28]   M. Nasr, R. Viter, C. Eid, R. Habchi, P. Miele, M. Bechelany, Enhanced photocatalytic performance of novel electrospun BN/TiO_2 composite nanofibers, New J. Chem. 41 (2016) 81–89. doi:10.1039/c6nj03088b.

[29]   R.T. Paine, C.K. Narula, Synthetic Routes to Boron Nitride, Chem. Rev. 90 (1990) 73–91. doi:10.1021/cr00099a004.

[30]   C. Zhou, C. Lai, C. Zhang, G. Zeng, D. Huang, M. Cheng, L. Hu, W. Xiong, M. Chen, J. Wang, Y. Yang, L. Jiang, Semiconductor/boron nitride composites: Synthesis, properties, and photocatalysis applications, Appl. Catal. B Environ. 238 (2018) 6–18. doi:10.1016/j.apcatb.2018.07.011.

[31]　J. Li, J. Lin, X. Xu, X. Zhang, Y. Xue, J. Mi, Z. Mo, Y. Fan, L. Hu, X. Yang, J. Zhang, F. Meng, S. Yuan, C. Tang, Porous boron nitride with a high surface area: hydrogen storage and water treatment, Nanotechnology. 24 (2013) 155603. doi:10.1088/0957-4484/24/15/155603.

[32]　J. Biscarat, M. Bechelany, C. Pochat-Bohatier, P. Miele, Graphene-like BN/gelatin nanobiocomposites for gas barrier applications, Nanoscale. 7 (2015) 613–618. doi:10.1039/c4nr05268d.

[33]　R. Abe, M. Higashi, K. Sayama, Y. Abe, H. Sugihara, Photocatalytic activity of R_3MO_7 and $R_2Ti_2O_7$ (R = Y, Gd, La; M = Nb, Ta) for water splitting into H_2 and O_2, J. Phys. Chem. B. 110 (2006) 2219–2226. doi:10.1021/jp0552933.

[34]　M.I. Zalas, M. Laniecki, Photocatalytic hydrogen generation over lanthanides-doped titania, in: Sol. Energy Mater. Sol. Cells, 2005: pp. 287–296. doi:10.1016/j.solmat.2005.02.014.

[35]　S.C. Mailley, A. Kelaidopoulou, A. Siddle, A.L. Dicks, P. Holtappels, C.E. Hatchweil, M. Mogensen, Electrocatalytic activity of a $Gd_2Ti_{0.6}M0_{1.2}Sc_{0.2}O_{7-\delta}$anode towards hydrogen and methane electro-oxidation in a solid oxide fuel cell, Ionics (Kiel). 6 (2000) 11–12.

[36]　K.M. Parida, A. Nashim, S.K. Mahanta, Visible-light driven Gd2Ti2O7/GdCrO3 composite for hydrogen evolution, Dalt. Trans. 40 (2011) 12839–12845. doi:10.1039/c1dt11517k.

[37]　H. Huang, Y. He, X. Du, P.K. Chu, Y. Zhang, A General and Facile Approach to Heterostructured Core/Shell $BiVO_4$/BiOI p-n Junction: Room-Temperature in Situ Assembly and Highly Boosted Visible-Light Photocatalysis, ACS Sustain. Chem. Eng. 3 (2015) 3262–3273. doi:10.1021/acssuschemeng.5b01038.

[38] H. Huang, X. Han, X. Li, S. Wang, P.K. Chu, Y. Zhang, Fabrication of multiple heterojunctions with tunable visible-light-active photocatalytic reactivity in BiOBr-BiOI full-range composites based on microstructure modulation and band structures, ACS Appl. Mater. Interfaces. 7 (2015) 482–492. doi:10.1021/am5065409.

[39] H. Rao, W.Q. Yu, H.Q. Zheng, J. Bonin, Y.T. Fan, H.W. Hou, Highly efficient photocatalytic hydrogen evolution from nickel quinolinethiolate complexes under visible light irradiation, J. Power Sources. 324 (2016) 253–260. doi:10.1016/j.jpowsour.2016.05.095.

[40] J. Rodríguez-Carvajal, Recent developments of the program FULLPROF, Comm. Powder Diffr. (IUCr). Newsl. 26 (2001) 12–19.

[41] L.W. Finger, D.E. Cox, A.P. Jephcoat, A Correction for powder diffraction peak asymmetry due to axial divergence, J. Appl. Crystallogr. 27 (1994) 892–900. doi:10.1107/S0021889894004218.

[42] A. Fajar, E. Kartini, H. Mugirahardjo, M. Ihsan, Crystallite Size and Microstrain Measurement of Cathode Material after Mechanical Milling using Neutron Diffraction Technique, Atom Indones. 36 (2010) 111–115. http://download.portalgaruda.org/article.php?article=51561&val=4151.

[43] H. Song, H. Jiang, X. Liu, G. Meng, Efficient degradation of organic pollutant with WO_x modified nano TiO_2 under visible irradiation, J. Photochem. Photobiol. A Chem. 181 (2006) 421–428. doi:10.1016/j.jphotochem.2006.01.001.

[44] W. Ouyang, M.J. Muñoz-batista, A. Kubacka, R. Luque, M. Fernández-garcía, Enhancing photocatalytic performance of TiO_2 in H_2 evolution via Ru co- catalyst deposition, Appl. Catal. B Environ. 238 (2018) 434–443. doi:10.1016/j.apcatb.2018.07.046.

[45] M.F. Oliveira, D. Suarez, J.C.B. Rocha, A.V.N. de Carvalho Teixeira, M.E. Cortés, F.B. De Sousa, R.D. Sinisterra, Electrospun nanofibers of polyCD/PMAA polymers and their potential application as drug delivery system, Mater. Sci. Eng. C. 54 (2015) 252–261.

[46] P. Joshi, L. Zhang, D. Davoux, Z. Zhu, D. Galipeau, H. Fong, Q. Qiao, Composite of TiO_2 nanofibers and nanoparticles for dye-sensitized solar cells with significantly improved efficiency, Energy Environ. Sci. 3 (2010) 1507–1510.

[47] P. Mishra, Y.P. Singh, H.P. Nagaswarupa, S.C. Sharma, Y.S. Vidya, S.C. Prashantha, H. Nagabhushana, K.S. Anantharaju, S. Sharma, Caralluma fi mbriata extract induced green synthesis , structural , optical and photocatalytic properties of ZnO nanostructure modi fi ed with Gd, J. Alloys Compd. 685 (2016) 656–669. doi:10.1016/j.jallcom.2016.05.044.

[48] Y.S. Vidya, K. Gurushantha, H. Nagabhushana, S.C. Sharma, K.S. Anantharaju, C. Shivakumara, D. Suresh, H.P. Nagaswarupa, S.C. Prashantha, M.R. Anilkumar, Phase transformation of ZrO_2:Tb^{3+}nanophosphor: Color tunable photoluminescence and photocatalytic activities, J. Alloys Compd. 622 (2015) 86–96. doi:10.1016/j.jallcom.2014.10.024.

[49] R.D. SHANNON, Revised Effective Ionic Radii and Systematic Studies of Interatomie Distances in Halides and Chaleogenides, Acta Cryst. 32 (1976) 751–767.

[50] S.M. Adyani, M. Ghorbani, A comparative study of physicochemical and photocatalytic properties of visible light responsive Fe, Gd and P single and tri-doped TiO_2 nanomaterials, J. Rare Earths. 36 (2018) 72–85. doi:10.1016/j.jre.2017.06.012.

[51] A.W. Xu, Y. Gao, H.Q. Liu, The preparation, characterization, and their photocatalytic activities of rare-earth-doped TiO_2 nanoparticles, J. Catal. 207 (2002) 151–157. doi:10.1006/jcat.2002.3539.

[52]   M. Saif, S.A. El-molla, S.M.K. Aboul-fotouh, M.M. Ibrahim, L.F.M. Ismail, D.C. Dahn, Nanostructured Gd^{3+}-TiO_2 surfaces for self-cleaning application, J. Mol. Struct. 1067 (2014) 120–126. doi:10.1016/j.molstruc.2014.03.024.

[53]   D. Toloman, A. Popa, M. Stefan, O. Pana, T.D. Silipas, S. Macavei, L. Barbu-Tudoran, Impact of Gd ions from the lattice of TiO_2 nanoparticles on the formation of reactive oxygen species during the degradation of RhB under visible light irradiation, Mater. Sci. Semicond. Process. 71 (2017) 61–68. doi:10.1016/j.mssp.2017.07.004.

[54]   H. Cai, X. Chen, Q. Li, B. He, Q. Tang, Enhanced photocatalytic activity from Gd , La codoped TiO_2 nanotube array photocatalysts under visible-light irradiation, Appl. Surf. Sci. 284 (2013) 837–842. doi:10.1016/j.apsusc.2013.08.018.

[55]   S. Sahoo, A.K. Arora, V. Sridharan, Raman line shapes of optical phonons of different symmetries in anatase TiO_2 nanocrystals, J. Phys. Chem. C. 113 (2009) 16927–16933. doi:10.1021/jp9046193.

[56]   M.P. Moret, R. Zallen, D.P. Vijay, S.B. Desu, Brookite-rich titania films made by pulsed laser deposition, Thin Solid Films. 366 (2000) 8–10. doi:10.1016/S0040-6090(00)00862-2.

[57]   T. Hirata, Pressure, temperature and concentration dependences of phonon frequency with variable Grüneisen parameter: Fits to the Raman-active Eg mode in TiO_2 and $Ti_{1-x}Zr_xO_2$ ($X \leq 0.1$), Phys. Status Solidi Basic Res. 209 (1998) 17–24. doi:10.1002/(SICI)1521-3951(199809)209:1<17::AID-PSSB17>3.0.CO;2-R.

[58]   L. Xu, X. Ma, N. Sun, F. Chen, Bulk oxygen vacancies enriched TiO_2 and its enhanced visible photocatalytic performance, Appl. Surf. Sci. 441 (2018) 150–155. doi:10.1016/j.apsusc.2018.01.308.

[59] L. Hou, M. Zhang, Z. Guan, Q. Li, J. Yang, Effect of annealing ambience on the formation of surface/bulk oxygen vacancies in TiO_2 for photocatalytic hydrogen evolution, Appl. Surf. Sci. 428 (2018) 640–647. doi:10.1016/j.apsusc.2017.09.144.

[60] X. Pan, M.Q. Yang, X. Fu, N. Zhang, Y.J. Xu, Defective TiO_2 with oxygen vacancies: Synthesis, properties and photocatalytic applications, Nanoscale. 5 (2013) 3601–3614. doi:10.1039/c3nr00476g.

[61] M. Pal, U. Pal, J.M.G.Y. Jiménez, F. Pérez-Rodríguez, Effects of crystallization and dopant concentration on the emission behavior of TiO_2: Eu nanophosphors, Nanoscale Res. Lett. 7 (2012) 1–12. doi:10.1186/1556-276X-7-1.

[62] W.F. Zhang, Y.L. He, M.S. Zhang, Z. Yin, Q. Chen, Raman scattering study on anatase TiO_2 nanocrystals, J. Phys. D-Applied Phys. 33 (2000) 912–916. doi:Doi 10.1088/0022-3727/33/8/305.

[63] N. Nithyaa, N. V Jaya, Structural, Optical, and Magnetic Properties of Gd-Doped TiO_2 Nanoparticles, J. Supercond. Nov. Magn. 31 (2018) 4117–4126. doi:10.1007/s10948-018-4693-9.

[64] X. Lv, J. Wang, Z. Yan, D. Jiang, J. Liu, Design of 3D h- BN architecture as Ag_3VO_4 enhanced photocatalysis stabilizer and promoter, "Journal Mol. Catal. A, Chem. 418–419 (2016) 146–153. doi:10.1016/j.molcata.2016.03.036.

[65] S. Paul, B. Choudhury, A. Choudhury, Magnetic property study of Gd doped TiO_2 nanoparticles, J. Alloys Compd. 601 (2014) 201–206. doi:10.1016/j.jallcom.2014.02.070.

[66] S. Paul, P. Chetri, B. Choudhury, G.A. Ahmed, A. Choudhury, Enhanced visible light photocatalytic activity of Gadolinium doped nanocrystalline titania : An experimental and theoretical study, J. Colloid Interface Sci. 439 (2015) 54–61.

doi:10.1016/j.jcis.2014.09.083.

[67] J. Mu, B. Chen, M. Zhang, Z. Guo, P. Zhang, Z. Zhang, Y. Sun, C. Shao, Y. Liu, Enhancement of the visible-light photocatalytic activity of In_2O_3-TiO_2 nanofiber heteroarchitectures, ACS Appl. Mater. Interfaces. 4 (2012) 424–430. doi:10.1021/am201499r.

[68] S. Obregón, A. Kubacka, M. Fernández-García, G. Colón, High-performance Er^{3+}-TiO_2 system: Dual up-conversion and electronic role of the lanthanide, J. Catal. 299 (2013) 298–306. doi:10.1016/j.jcat.2012.12.021.

[69] S. Song, C. Wang, F. Hong, Z. He, Q. Cai, J. Chen, Gallium- and iodine-co-doped titanium dioxide for photocatalytic degradation of 2-chlorophenol in aqueous solution : Role of gallium, Appl. Surf. Sci. 257 (2011) 3427–3432. doi:10.1016/j.apsusc.2010.11.040.

[70] A.S. Nazarov, V.N. Demin, E.D. Grayfer, A.I. Bulavchenko, A.T. Arymbaeva, H.J. Shin, J.Y. Choi, V.E. Fedorov, Functionalization and dispersion of hexagonal boron nitride (h-BN) nanosheets treated with inorganic reagents, Chem. - An Asian J. 7 (2012) 554–560. doi:10.1002/asia.201100710.

[71] J. Liqiang, S. Xiaojun, X. Baifu, W. Baiqi, C. Weimin, F. Hongganga, The preparation and characterization of La doped TiO_2 nanoparticles and their photocatalytic activity, J. Solid State Chem. 177 (2004) 3375–3382. doi:10.1016/j.jssc.2004.05.064.

[72] C. Lv, Y. Zhou, H. Li, M. Dang, C. Guo, Y. Ou, B. Xiao, Synthesis and characterisation of Gd^{3+} -doped mesoporous TiO_2 materials, Appl. Surf. Sci. 257 (2011) 5104–5108. doi:10.1016/j.apsusc.2011.01.029.

[73] T. Xiong, F. Dong, Z. Wu, Enhanced extrinsic absorption promotes the visible light

photocatalytic activity of wide band-gap $(BiO)_2CO_3$ hierarchical structure, RSC Adv. 4 (2014) 56307–56312. doi:10.1039/c4ra10786a.

[74] S.P. Sahu, S.L. Cates, H. Il Kim, J.H. Kim, E.L. Cates, The Myth of Visible Light Photocatalysis Using Lanthanide Upconversion Materials, Environ. Sci. Technol. 52 (2018) 2973–2980. doi:10.1021/acs.est.7b05941.

[75] K. Alamelu, V. Raja, L. Shiamala, B.M.J. Ali, Biphasic TiO_2 nanoparticles decorated graphene nanosheets for visible light driven photocatalytic degradation of organic dyes, Appl. Surf. Sci. 430 (2018) 145–154. doi:10.1016/j.apsusc.2017.05.054.

[76] P.A.K. Reddy, C. Manvitha, P.V.L. Reddy, K.H. Kim, V.D. Kumari, Enhanced hydrogen production activity over BiO_X–TiO_2 under solar irradiation: Improved charge transfer through bismuth oxide clusters, J. Energy Chem. 26 (2017) 390–397. doi:10.1016/j.jechem.2016.12.007.

[77] W.Y. Cheng, T.H. Yu, K.J. Chao, S.Y. Lu, Cu_2O-decorated mesoporous TiO_2 beads as a highly efficient photocatalyst for hydrogen production, ChemCatChem. 6 (2014) 293–300. doi:10.1002/cctc.201300681.

[78] S. Escobedo, B. Serrano, H. De Lasa, Environmental Quantum yield with platinum modified TiO_2 photocatalyst for hydrogen production, "Applied Catal. B, Environ. 140–141 (2013) 523–536. doi:10.1016/j.apcatb.2013.04.016.

[79] O. Fontelles-Carceller, M.J. Muñoz-Batista, E. Rodríguez-Castellón, J.C. Conesa, M. Fernández-García, A. Kubacka, Measuring and interpreting quantum efficiency for hydrogen photo-production using Pt-titania catalysts, J. Catal. 347 (2017) 157–169. doi:10.1016/j.jcat.2017.01.012.

[80] J.F. Guayaquil-sosa, B. Serrano-rosales, P.J. Valadés-pelayo, H. De Lasa, Photocatalytic

hydrogen production using mesoporous TiO_2 doped with Pt, "Applied Catal. B, Environ. 211 (2017) 337–348. doi:10.1016/j.apcatb.2017.04.029.

[81] X. Li, J. Zhao, J. Yang, Semihydrogenated BN sheet: A promising visible-light driven photocatalyst for water splitting, Sci. Rep. 3 (2013) 3–7. doi:10.1038/srep01858.

[82] R. Imani, R. Dillert, D.W. Bahnemann, M. Pazoki, T. Apih, V. Kononenko, N. Repar, V. Kralj-Iglič, G. Boschloo, D. Drobne, T. Edvinsson, A. Iglič, Multifunctional Gadolinium-Doped Mesoporous TiO_2 Nanobeads: Photoluminescence, Enhanced Spin Relaxation, and Reactive Oxygen Species Photogeneration, Beneficial for Cancer Diagnosis and Treatment, Small. 13 (2017) 1–11. doi:10.1002/smll.201700349.

[83] Z. Zhao, Q. Liu, Effects of lanthanide doping on electronic structures and optical properties of anatase TiO_2 from density functional theory calculations, J. Phys. D. Appl. Phys. 41 (2008). doi:10.1088/0022-3727/41/8/085417.

[84] S. Meng, X. Ye, X. Ning, M. Xie, X. Fu, S. Chen, Selective oxidation of aromatic alcohols to aromatic aldehydes by BN/metal sulfide with enhanced photocatalytic activity, "Applied Catal. B, Environ. 182 (2016) 356–368. doi:10.1016/j.apcatb.2015.09.030.

[85] V. Štengl, M. Slušná, h-BN-TiO_2 Nanocomposite for Photocatalytic Applications, J. Nanomater. 2016 (2016). doi:10.1155/2016/4580516.

[86] M. Ni, M.K.H. Leung, D.Y.C. Leung, K. Sumathy, A review and recent developments in photocatalytic water-splitting using TiO_2 for hydrogen production, Renew. Sustain. Energy Rev. 11 (2007) 401–425. doi:10.1016/j.rser.2005.01.009.